Fano fluctuations in superconducting-nanowire single-photon detectors

A. G. Kozorezov, C. Lambert, F. Marsili, M. J. Stevens, V. B. Verma, J. P. Allmaras, M. D. Shaw, R. P. Mirin, and Sae Woo Nam

Fano fluctuations in superconducting nanowire single-photon detectors

A. G.Kozorezov[1], C. Lambert[1], F. Marsili[2], M. J. Stevens[3], V. B. Verma[3], J.P.Allmaras[2], M. D. Shaw[2], R. P. Mirin[3], Sae Woo Nam[3]

[1]*Department of Physics, Lancaster University, Lancaster, UK,*
[2] *Jet Propulsion Laboratory, California Institute of Technology,*
4800 Oak Grove Dr., Pasadena, California 91109, USA,
[3]*National Institute of Standards and Technology, 325 Broadway, Boulder, CO 80305, USA*
(Dated: July 21, 2017)

Because of their universal nature, Fano fluctuations are expected to influence the response of superconducting nanowire single-photon detectors (SNSPDs). We predict that photon counting rate (PCR) as a function of bias current (I_B) in SNSPDs is described by an integral over a transverse coordinate-dependent complementary error function. Fano fluctuations in the amount of energy deposited into the electronic system contribute to the finite width of this error function, ΔI_B. The local response of an SNSPD can also affect this width: the location of the initial photon absorption site across the width of the wire can impact the probability of vortex-antivortex unbinding and vortex entry from the edges. In narrow-nanowire SNSPDs, the local responses are uniform, and Fano fluctuations dominate ΔI_B. We demonstrate good agreement between theory and experiments for a series of bath temperatures and photon energies in narrow-wire WSi SNSPDs. In a wide-nanowire device, the strong local dependence will introduce a finite width to the PCR curve, but with sharp cusps. We show how Fano fluctuations can smooth these features to produce theoretical curves that better match experimental data. We also show that the time-resolved hotspot relaxation curves predicted by Fano fluctuations match the previously measured Lorentzian shapes (except for their tails) over the entire range of bias currents investigated experimentally.

I. INTRODUCTION

The conversion of light into detectable excitations constitutes the key process in photodetection. Understanding energy flow and relaxation pathways is highly relevant in a wide variety of devices, from traditional scintillators[1] to new graphene-based materials[2,3]. The efficiency of detection depends on the competition between multiple energy flow pathways.

Fano fluctuations describe variations in the number of charge carriers generated in a single-particle or single-photon sensor. Upon impact with a particle or absorption of a photon, energy is deposited in the sensor. This energy is partitioned between charged and neutral elementary excitations, for example between electrons and phonons. Fano fluctuations are caused by the branching processes and result in variations in the fraction of energy deposited in each system. Fano fluctuations are known to determine the theoretical limit of spectral resolution of many types of spectrometers, and are a limiting factor in the noise characteristics of CCDs and CMOS image sensors[4,5], as well as superconductor sensors such as superconducting tunnel junctions and microwave kinetic inductance detectors[6–8]. Fano fluctuations may also be significant in sensors lacking an energy gap in the spectrum of elementary excitations, for example in superconducting transition edge microcalorimeters grown on a solid substrate[9–11] and magnetic microcalorimeters[12,13]. The relevant parameter of the detector material is the Fano factor, which quantifies the branching variance: a smaller factor indicates better resolving power.

To date, the role of Fano fluctuations in SNSPDs has not been discussed in the literature, likely because it was viewed as irrelevant. It has generally been assumed that an ideal SNSPD should exhibit sharp spectral and current thresholds for photodetection, characterized by a step function in detection efficiency when plotted as a function of bias current[14]. The broadening of this step function into the sigmoidal shape observed in experiments has been attributed to inhomogeneities in nanowire width or thickness, or to variations in the position of the photon absorption site. This latter variation affects the competing probabilities of vortex entry at the edge of the wire and unbinding of vortex-antivortex pairs away from the edge[15–23].

Here, we present a study of the influence of Fano fluctuations on the current and spectral dependence of the detection efficiency of SNSPDs. We show that a sigmoidal shape is expected even in the absence of these inhomogeneities. The energy deposited into the electronic system by monochromatic photons fluctuates about the mean value due to the partition between quasiparticles (QP) and phonons. This occurs during energy downconversion, with a variance given by the Fano factor. We show that photon counting rate vs. bias current in SNSPDs in general is described by an integral over a transverse coordinate-dependent complementary error function with a width ΔI_B determined by the variance of Fano fluctuations.
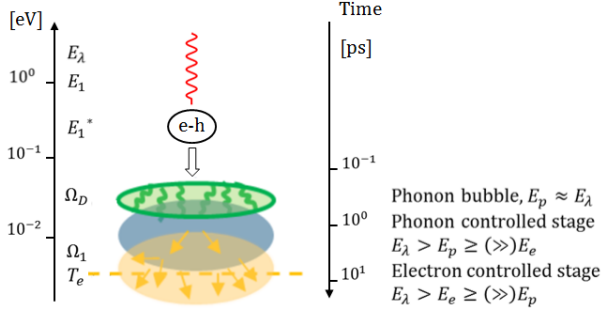
FIG. 1: Schematic picture of photoelectron-hole energy down-conversion cascade in a metal.

FIG. 2: Calculated electron-electron, τ_{ee}^{-1}, electron-phonon, τ_{ep}^{-1}, and phonon-electron, τ_{pe}^{-1}, scattering rates vs excitation energy in WSi and NbN. Each rate is normalized to the characteristic time τ_0 of the corresponding material, and energy is shown in units of the material's critical temperature T_C. Above the threshold energy Ω_1 (and below E_1^*), phonon emission dominates energy loss. Below Ω_1, electron-electron scattering and phonon absorption dominate. The Debye energy, Ω_D, is at the right edge of each plot, while the other thresholds, E_1 and E_1^*, occur at much higher energies (not shown).

II. FANO FLUCTUATIONS IN SNSPDS

A. Energy down-conversion cascade

We start by describing the first moments following the absorption of a photon in the SNSPD. We use the picture of energy down-conversion developed in our early work[24] for thick and clean films. In contrast, the electron elastic mean free paths in the typical thin ($\sim$5 nm thick) disordered films used for SNSPDs are more than three orders of magnitude smaller than in the $\sim$300-600 nm-thick films used in superconducting tunnel junctions or superconducting transition edge sensors. Although the essential picture of down-conversion remains conceptually the same, the disorder in thin (2D) films strongly influences electron-electron, electron-phonon and phonon-electron scattering, affecting at least some of the essential energy thresholds and time scales. Fig.1 schematically illustrates the evolving energy down-conversion cascade following the absorption of a visible or infrared photon. At $t = 0$, a photon is absorbed and an electron-hole pair is generated. The sum of electron and hole energies is equal to the photon energy, E_λ. On average, assuming the electron density of states is constant near the Fermi energy E_F on the scale $E_\lambda \ll E_F$, half this energy is given to the electron and half to the hole.

The energy and time scales in Fig.1 illustrate absorption of a visible photon. There are several characteristic energy thresholds describing the energy down-conversion cascade. E_λ corresponds to the maximum energy of electronic (electron or hole) excitations. The primary electronic excitations relax by interacting with other electrons via electron-electron scattering (at a rate $\tau_{ee}^{-1}(\epsilon) \propto \epsilon^2$) or by emitting phonons (electron-phonon interaction at a rate $\tau_{ep}^{-1}(\epsilon)$). Both rates depend on the electron energy, ϵ.

Early on, when the excitation energy is still much greater than the Debye energy (Ω_D), electron-electron scattering dominates the relaxation, whereas τ_{ep} maintains the constant value τ_s for all $\epsilon > \Omega_D$. Very quickly, the electron loses enough energy to reach the threshold energy E_1, at which the two rates are equal: $\tau_{ee}(E_1) =$
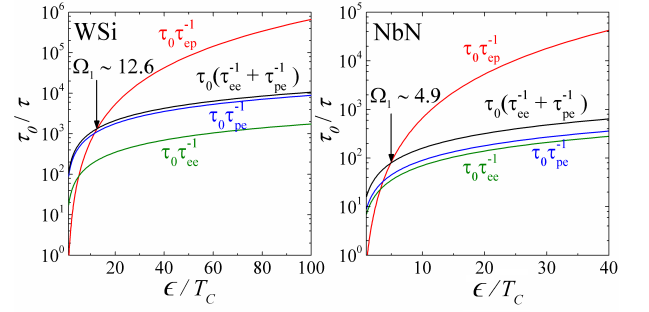
$\tau_{ep}(E_1) = \tau_s$. Below E_1, which is typically close to 1 eV[24], the phonon emission rate becomes higher than the electron-electron scattering rate. Nonetheless the latter still controls energy relaxation, because the maximum energy lost per phonon emitted is limited to $\sim \Omega_D$, whereas an electron can lose a substantial fraction of its energy upon scattering with another electron.

As each electron loses energy, eventually τ_{ee}^{-1} slows down enough, and the energy lost per electron-electron scattering event becomes small enough, that electron-phonon interactions start to dominate energy loss. The threshold energy at which this crossover occurs is called E_1^*. The phonon-dominated stage that starts below E_1^* lasts until the mean energies of interacting electrons and phonons reach the lower threshold, Ω_1. This latter threshold is defined as the energy at which $\tau_{ep}^{-1}(\Omega_1) = \tau_{pe}^{-1}(\Omega_1) + \tau_{ee}^{-1}(\Omega_1)$, where τ_{pe}^{-1} is the phonon absorption rate. This second crossover energy is illustrated in Fig.2, which plots characteristic relaxation times in WSi and NbN as a function of quasiparticle energy calculated from the Fermi energy for energies up to the Debye energies ($\sim 100 T_C$ in WSi, $\sim 40 T_C$ in NbN).

Below Ω_1 (which is usually $\ll \Omega_D$), electron-electron and phonon-electron interactions in the disordered film gain control over relaxation. As Fig.2 shows, this happens because the phonon emission rate $\tau_{ep}^{-1}(\epsilon)$ for $\epsilon < \Omega_D$ decreases with energy faster than the rate of electron-electron scattering $\tau_e^{-1}(\epsilon)$ (which is now dominated by interactions with small momentum transfer due to strong elastic scattering of electrons in a disordered film) and phonon absorption rate $\tau_{pe}^{-1}(\epsilon)$.

Each characteristic time plotted in Fig.2 is the lifetime of a single excited state (scattering-out time) describing relaxation of a test particle, considering transitions to all possible final states. The electron-electron

scattering time as a function of energy was calculated from Altshuler and Aronov's formula for a disordered 2D normal metal[25], while electron-phonon and phonon-electron scattering times were taken from Chang[26]. Note that the expressions for electron-phonon and phonon-electron times were taken neglecting vertex renormalisation by strong disorder, which is valid for the range of energies $\epsilon l/\hbar c \geq 1$, where l is the elastic mean free path for electrons and c is the sound velocity[27,28]. This inequality holds true for higher energies, while at lower energies, close to Ω_1, the role of disorder becomes important. The characteristic time τ_0 entering the expressions for electron-phonon and phonon-electron scattering times depends on the electron-phonon coupling strength and is taken for WSi and NbN to be 5-10 and 0.3-0.6 ns, respectively. These numbers fall into the expected range for the pure metal limit. They are consistent with the magnitudes of the Debye energies and critical temperatures of NbN and WSi and with the median values for the effective coupling strengths[29]. As follows from Fig.2, in both NbN and WSi the electron-phonon interaction dominates down-conversion over a significant range of energies. This means that the loss of high-frequency, non-equilibrium (athermal) phonons from the thin film, with thickness comparable to phonon mean free paths, may be significant.

Between E_1 and Ω_1, by definition $\tau_{ee}(\epsilon) > \tau_s$. The energy relaxation time for the initial electron-hole pair due to electron-electron interactions with electrons of the Fermi distribution at equilibrium is longer than $\tau_{ee}(\epsilon)$. The energy relaxation time can be roughly estimated from the expression:[25]

$$
\begin{aligned}
\frac{1}{\tau_{ee}}(\epsilon) &\propto \int_0^\epsilon \mathrm{d}\omega \int_0^\omega \mathrm{d}\epsilon' \int_0^\infty \mathrm{d}q q^2 W_q \frac{1}{qV_F} \\
\dot\epsilon &\propto \int_0^\epsilon \mathrm{d}\omega\omega \int_0^\omega \mathrm{d}\epsilon' \int_0^\infty \mathrm{d}q q^2 W_q \frac{1}{qV_F} \\
\dot\epsilon &= -\frac{2}{3}\frac{\epsilon}{\tau_{ee}(\epsilon)}
\end{aligned}
\tag{1}
$$

where ω and q are the energy and momentum transfer at the collision, ϵ' is the energy of a particle the electron collides with, W_q is the matrix element describing the interaction, and V_F is the Fermi velocity. Solving the last equation yields

$$
\frac{\epsilon(t)}{\epsilon_0} = \left[1 + \frac{4}{3}\frac{t}{\tau_{ee}(\epsilon_0)}\right]^{-1/2},
\tag{2}
$$

where $\epsilon_0 = \epsilon(0)$. Equation (2) predicts that an electron with energy ϵ loses half that energy in a time $\frac{9}{4}\tau_{ee}(\epsilon)$. By comparison, losing the same amount of energy due to sequential emission of phonons takes $\sim (\epsilon/2\Omega_D)\tau_s$. By definition, these two times are equal at the threshold energy $E_1^* = E_1 \left(\frac{9}{2}\frac{\Omega_D}{E_1}\right)^{1/3}$. This assumes the e-e scattering close to E_1^* is dominated by large momentum transfer, which is true provided that $\tau_{ee}^{-1}(\epsilon)$ from Fig.2 extrapolated to E_1^* (according to a linear law) remains smaller

than the inelastic scattering rate. Thus, disorder does not affect the threshold E_1^* if $(E_1^*/\Omega_D)^2 \leq 2\tau_{ee}(\Omega_D)/\tau_s$ (recall that $\tau_{ep}(\Omega_D) = \tau_s$). As seen in Fig.2, this condition is fulfilled for WSi. For NbN, the effect of disorder on the threshold E_1^* is stronger, pushing E_1^* towards somewhat lower values. In all situations where $E_1^* \gg \Omega_D$, electron-phonon scattering is the dominant mechanism of electron/hole energy relaxation for the range of energies $\Omega_1 < \epsilon < E_1^*$.

With $E_1 \sim 1$ eV and $\Omega_D \sim 30$ meV, we obtain $E_1^* \sim 500$ meV for typical materials. When ϵ is close to E_1^*, subsequent cooling proceeds mostly via sequential emission of phonons. Since the characteristic values for τ_s are tens of femtoseconds, unless the materials have a small Debye energy, cooling from 500 meV down to Ω_D will last a fraction of a picosecond. By the end of this cooling, which completes before the lifespan of the first emitted phonons, most of the photon energy has been transferred to high energy (Debye) phonons. It is convenient to consider this highly non-equilibrium state as the natural initial condition for the subsequent evolution of interacting quasiparticles and phonons. In Fig.1 this condition is called a phonon bubble.

To summarize, upon absorption, all the photon energy is transferred to one electron-hole pair. Initially, electron-electron interactions dominate the down-conversion, and this energy is quickly redistributed to a large number of electronic excitations (for $E_\lambda \gg E_1^*$). Below the threshold energy E_1^*, phonon emission dominates the relaxation, and most of the energy is transferred to phonons, creating a "phonon bubble." The resulting phonon-controlled stage evolves via several down-converting generations of vibrational excitations until the next energy threshold, Ω_1, is reached. Below Ω_1, electron-electron scattering and phonon absorption dominate over phonon emission, and energy is quickly transferred back to the electronic system. The subsequent electron-controlled stage then evolves by redistributing this energy within the electronic system until reaching a quasi-equilibrium, described by the temperature T_e. Fig.1 illustrates typical times when these thresholds are reached.

B. Hot belt formation

Upon completion of the down-conversion cascade described in the previous section, a fraction of the photon energy, $E < E_\lambda$, remains in the electronic system and a hotspot is created[24]. For a thin, narrow wire, we assume the hotspot spans the width of the wire, W, forming a hot belt[30,31]. This hot belt occupies a volume $V_{HS} = WL_{HS}d$, where $L_{HS} \geq W$ is the hotspot length along the wire and d is the wire thickness. In this situation, L_{HS} can be determined in tomography experiments[30]. We assume that after completion of the cascade, the quasiparticle distribution is thermalized, owing to a strong electron-electron interaction in the dis-

ordered nanowire. Therefore, we assume that after the absorption of a photon, the QP temperature instantly increases from the bath temperature, T_b, to the excitation temperature, T_{ex}. The hotspot excitation temperature is determined from the thermal balance

$$E_{HS}(I_B, T_{ex}, B) - E_{HS}(I_B, T_b, B) = \int_{T_b}^{T_{ex}} dT'$$

$$C(T', I_B, B) = E_{HS}^{QP}(I_B, T_{ex}, B) - E_{HS}^{QP}(I_B, T_b, B) +$$

$$2N(0)V_{HS}k_B \int_{-\infty}^{\infty} d\xi \int_{T_{ex}^{-1}}^{T_b^{-1}} d\beta \frac{1}{\exp(\beta\epsilon) + 1} \frac{\partial \epsilon}{\partial \beta} = E \quad (3)$$

where $E_{HS}(I_B, T, B)$ is the internal energy of the hotspot, $C(T, I_B, B)$ is the electronic specific heat of the superconducting wire as a function of temperature, current and magnetic field, $N(0)$ is the normal state density of states at the Fermi level per spin, $\epsilon = \sqrt{\xi^2 + \Delta^2(I_B, T, B)}$ is the quasiparticle energy, Δ is the order parameter in the current-carrying nanowire, B is the external magnetic field and E the actual amount of energy deposited in the electronic system. The energy of quasiparticle distribution in the hotspot is

$$E_{HS}^{QP}(I_B, T, B) = 4N(0)V_{HS} \int_0^{\infty} d\epsilon \frac{\epsilon \rho(\epsilon, I_B, T, B)}{\exp(\epsilon/T) + 1} \quad (4)$$

Here $\rho(\epsilon, T, I_B, B)$ is the density of states within the hotspot in units of $N(0)$. The dependencies on bias current I_B, temperature T and magnetic field B originate from the pair-breaking energy and the order parameter being functions of T, I_B and B. The last term in the expression (3) originates from the dependence of QP dispersion relations in the hotspot on temperature.

In an ideal SNSPD there is a count event every time the energy E exceeds the threshold E^*, determined from

$$E_{HS}(I_B, T_b, B) + E^* = E_{HS}(I_B, T_s, B) \quad (5)$$

where T_s is the temperature at which the hotspot undergoes a transition from the superconducting to the normal state. This temperature depends on bias current and external magnetic field; for a narrow wire, it can be found using the solution of the Usadel equation for density of states[32] and the dependence of the order parameter on current, temperature and magnetic field[30,31,33,34].

In wider wires, the characteristic shape of a hotspot is more complicated. If the photon absorption site is far from the edge of the wire, then the hotspot can be cylindrical. If its radius, R_{HS}, is smaller than half the wire width, $W > 2R_{HS} \gg d$, the hotspot will not span the width of the wire, and its creation will result in a current density redistribution. The details of this redistribution will depend on the location of the absorption site, described by the lateral coordinate y. In very thick wires, the hotspot may be spherical (or close to semi-spherical for shallow absorption), with a radius $R_{HS} \ll \min\{d, W\}$, and the geometry of current redistribution becomes three-dimensional.

In wide, thin nanowires, the change in the current flow facilitates vortex entry at the edges of the nanowire or unbinding of vortex-antivortex pairs. In this situation, Fano fluctuations result in supercurrent density fluctuations, and their description becomes more complicated. The fluctuating order parameter, current density and temperature in the hotspot become dependent on the coordinate of the absorption site and are connected through a more complicated relation. The coordinate-dependent detection current, $I_{det}(y, E, T_b, B)$ is introduced through the appropriate simulation[16,19], and the implicit condition for the E^* threshold to trigger the detection click can be written as

$$I_B = I_{det}(y, T^*, T_b, B) = I_{det}(y, E^*, T_b, B) \quad (6)$$

where $T^* = T(E^*)$ is the threshold temperature of the hotspot corresponding to energy deposition E^*.

C. Modeling Fano fluctuations

Fano fluctuations have been well studied in other types of superconducting sensors such as superconducting tunnel junctions and superconducting transition edge microcalorimeters. Following the absorption of monochromatic photons (at soft x-ray energies and below), pulse height spectra distributions in these devices are close to ideal Gaussians. This reflects the large number of quasiparticles generated and small statistical fluctuations[8,9]. For this reason, we choose to model Fano fluctuations in SNSPDs as a normalized Gaussian probability distribution describing energy deposition into the electronic system:

$$P(E) = \frac{1}{\sqrt{2\pi}\sigma} \exp\left[-\frac{(E - \bar{E})^2}{2\sigma^2}\right]. \quad (7)$$

The distribution is centered around a mean value $\bar{E} = \bar{\chi}E_\lambda$, where $\bar{\chi}$ is the average value of the photon yield, defined as $\chi = E/E_\lambda$, the ratio of the energy deposited in the hotspot after the absorption of a photon (E) to the photon energy (E_λ). The full width at half maximum of the distribution $P(E)$ is $2\sqrt{2\ln 2}\sigma$, where σ is the variance.

Since a count occurs when $E \geq E^*$, simple integration yields the normalized PCR for a narrow wire in the form

$$PCR^{NW} = \int_{E^*}^{\infty} dE P(E) = \frac{1}{2}\text{erfc}\left(\frac{E^* - \bar{E}}{\sqrt{2}\sigma}\right)$$

$$= \frac{1}{2}\text{erfc}\left[\frac{E_{HS}(I_B, T_s, B) - E_{HS}(I_B, T_b, B) - \bar{E}}{\sqrt{2}\sigma}\right] (8)$$

For a wide wire, a photon count occurs if the bias current exceeds the minimum detection current, which is a function of the coordinate y across the wire and depends on hotspot temperature (deposited energy),

bath temperature, magnetic field and photon wavelength: $I_{det}(y, T(E), T_b, B) = I_{det}(y, E, T_b, B)$. In this situation

$$PCR^{WW} = \int_0^\infty dE P(E) \frac{1}{W} \int_{-W/2}^{W/2} dy \Theta [I_B -$$

$$I_{det}(y, E, T_b, B)] = \int_0^\infty dE P(E) w(E, T_b, B) =$$

$$\frac{1}{W} \int_{-W/2}^{W/2} dy \, \text{erfc} \left[\frac{I_B - I_{det}(y, \bar{\chi} E_\lambda, T_b, B)}{\sqrt{2} \sigma I'_{det}(y, \bar{\chi} E_\lambda, T_b, B)} \right] \quad (9)$$

where $\Theta(x)$ is the Heaviside function, $w(E, T_b, B)$ is the fraction of the wire width where generation of a vortex results in formation of a normal domain across the wire, and $I'_{det}(y, \bar{\chi} E_\lambda, T_b, B) = \partial I_{det}(y, E, T_b, B) / \partial E|_{E=\bar{\chi} E_\lambda}$

Note that our model assumes a uniform spatial profile of absorption sites across the wire, which is obviously an over-simplification. The absorption probability can change near the edge of a nanowire, and this change will depend on the polarization of the incident photon. In a more complete treatment, Eq. (9) could be modified to account for this.

The total variance due to Fano fluctuations is determined from two statistically independent processes as $\sigma^2 = \sigma_1^2 + \sigma_2^2$. Following photon absorption, a rapid process of energy down-conversion is initiated, engaging numerous electronic and phonon excitations. Phonons can be divided into two groups. Non-pair-breaking phonons with energy $\hbar\Omega$ smaller than twice the order parameter 2Δ are decoupled from the condensate and can only be reabsorbed by excited QPs. In thin films, we neglect reabsorption, assuming the re-absorption time to be considerably longer than their escape into a substrate or thermalization time. In contrast, higher-energy phonons can break Cooper pairs and exchange energy with the electronic system. In a bulk superconductor, if the distance from the absorption site to the escape interface far exceeds the phonon mean free path, none of the pair-braking phonons escapes into the thermal bath before QPs thermalise.

By the end of down-conversion, the energy of a photon splits between QPs and non-pair-breaking phonons. σ_1 describes statistical fluctuations of E originating from fluctuations in the number of pair-breaking phonons under the assumption that none of the pair-breaking phonons from the down-conversion cascade escapes. It can be written $\sigma_1^2 = F \varepsilon E_\lambda$, where 2ε is the mean energy necessary to generate one pair of QPs. The Fano factor in most superconductors is $F \simeq 0.2$.[6,7] In superconducting films with thickness comparable to the mean free path of pair-breaking phonons, some of the highly energetic (athermal) phonons will escape. Thus, E_λ is replaced by $E' = (1 - \chi_a) E_\lambda$, where we introduce $0 < \chi_a < 1$ to account for the average fraction of athermal phonons escaping from the nanowire prior to the random partition of energy between QPs and non-pair-breaking phonons. In this more general case, $\sigma_1^2 = F \varepsilon (1 - \chi_a) E_\lambda$.

Energy loss from the film due to escaping athermal phonons is a random process, depending on the mean free path of each phonon and the probability of transmission into the substrate. This results in a second independent contribution to the variance, $\sigma_2^2 = J(E_\lambda) \varepsilon E_\lambda$, which we refer to as phonon down-conversion noise[10,11,35]. Note that J describes fluctuations in χ_a. If all athermal phonons are re-absorbed in the film, which is the case for thick films illuminated from the top, then $\chi_a = 0$ and $\sigma_2 = 0$ and the variance due to Fano fluctuations is simply $\sigma^2 = F \varepsilon E_\lambda$. In thin films, by contrast, accurate determination of the Fano factor $J(E_\lambda)$ is not an easy problem. It involves evaluation of statistical fluctuations of loss from successive generations of athermal phonons, which are part of an evolving distribution during the down-conversion process. We may, however, derive the lower limit to $J(E_\lambda)$ by ignoring contributions from lower-energy, longer-lived phonons from later generations. Although these later-generation phonons account for the majority of energy loss, they do not contribute substantially to *fluctuations* in energy loss: as the number of phonons increases, the mean energy per phonon decreases, leading to smaller fluctuations in energy loss. As a result, we take $J(E_\lambda) \approx J^1(E_\lambda)$, where the superscript 1 signifies that the latter quantity contains contributions only from phonons of the first generation, the phonon bubble.

In a thin film, photons are absorbed homogeneously through the depth of the film, and, similarly, first-generation phonons are also homogeneously generated as the energetic photoelectron or hole performs a random walk in the film. In the thin-film limit $(d \to 0)$ the Fano-factor $J^1(E_\lambda)$ does not depend on photon energy and can be written in the form[35]

$$J^1 = 2 \frac{\Omega_D}{\varepsilon} \frac{l_{pe,D}}{d} \int_{\cos(\theta_c)}^1 d\xi \xi \eta(\xi) \left\{ \frac{1}{4} \left(\frac{l_{pe,D}}{d} \right)^4 - \int_0^{d/l_{pe,D}\xi} dx x^3 \left[e^{-x} + \frac{1}{2} \eta(\xi) \sin^2(\theta_c/2) \left(1 - e^{-2x} \right) \right] \right\} \quad (10)$$

Here θ_c is the angle of total internal reflection; phonons that impinge the escape interface at larger angles stay inside the plane parallel film until they undergo scattering-assisted conversion and move at smaller angles $\theta < \theta_c$. η is the phonon transmission coefficient through the interface with the substrate for incidence below the critical angle and $l_{pe,D}$ is the mean free path of Debye phonons with respect to absorption by electrons. In addition, Ω_D is the dominant phonon energy in the phonon bubble; $l_{pe,D}/d$ is the probability of survival until reaching the escape interface; and the inner integral denotes an average of phonon contributions over the distribution, accounting for their probabilities to reach the interface depending on energy and angle of incidence.

Equation (10) reflects that the variance in the number of phonons emitted into the critical cone from any energy interval follows a binomial distribution, where the contributions from phonons of different energies are sta-

tistically independent. The total variance is the integral over contributions from individual groups of phonons from the flat distribution of first-generation phonons. Note that a binomial distribution is close to the normal distribution in Eq. (7) under the assumption of large phonon numbers in each energy interval. Thus, integration over the spectrum works well for phonons of later generations. For first-generation phonons it works for the dominant phonon group with energies close to the Debye energy. The second integral in Eq. (10) is an approximation of the dominant phonon contribution.

The *total* variance due to Fano noise can be written

$$\sigma^2 = \sigma_1^2 + \sigma_2^2 = F_{eff}\varepsilon E_\lambda, \tag{11}$$

where the effective Fano factor is

$$F_{eff} = F(1 - \chi_a) + J^1. \tag{12}$$

Our estimate of F_{eff} relies on using the simplest model (Debye) of one phonon mode with a linear dispersion relation. For phonons of the first few generations, $\epsilon l/\hbar c \geq 1$, and our estimate of J^1 is not affected by disorder. Given these approximations, this estimate provides only a rough indication of the magnitude of the effect.

In the next section, we compare our simulation with experiments on WSi SNSPDs, using F_{eff} as a fitting parameter. Because of the large acoustic mismatch between WSi and the SiO_2 substrate, even for normal incidence we have $\eta \leq 0.5$. Taking $\eta = 0.5$ for WSi on an amorprhous SiO_2 substrate we obtain $1.0 \leq J^1 \leq 1.5$ for $5 \leq \tau_0 \leq 10$ ns. For NbN on SiO_2, a similar calculation yields $0.8 \leq J^1 \leq 1.0$ for $0.5 \leq \tau_0 \leq 1.0$ ns. With these estimates, we conclude that phonon downconversion noise dominates Fano fluctuations ($\sigma_2 \gg \sigma_1$) and $F_{eff} \approx J^1$. This is not surprising, because the fluctuations in the number of phonons falling within the escape cone and the fluctuations of the ultimate number of quasiparticles are both proportional to the square root of the respective mean numbers. Fluctuations for athermal phonons are strong, partly because of their large energies and hence smaller numbers, but more importantly because only a significantly smaller fraction of all athermal phonons (those within the escape cone) contribute to fluctuations in the energy loss. Subsequent phonon generations also contribute to fluctuations, increasing σ_2, although each subsequent contribution becomes smaller, because the number of phonons doubles in each subsequent generation. Thus, even if we overestimated J^1, there is still an extra contribution from lower-energy phonons, and $\sigma_2 \gg \sigma_1$. Because we cannot provide credible estimates for contributions to the overall variance from later phonon generations, we will use F_{eff} as a fitting parameter. The likely range of variation of F_{eff} must be consistent with our estimate for J^1.

D. The effect of Fano fluctuations on the shape of PCR curves in narrow, homogeneous SNSPDs

The shape of a PCR curve vs bias current at fixed values of T_b, λ and B is affected by the bias dependence of the energy terms in Eq. (8): $E(I_B, T_s, B) - E(I_B, T_b, B) - \bar{E}$. In addition, both σ_1 and σ_2 depend on bias current: σ_1 depends on the order parameter at the critical point Δ_s, while contributions to σ_2 from phonons of later generations may weakly depend on the threshold energy Ω_1, because both Δ_s and Ω_1 depend on I_B. We define the *cutoff current* of the SNSPD at a fixed wavelength, bath temperature, and magnetic field, $I_{co}(\lambda, T_b, B)$, as the inflection point of the PCR vs I_B curve and use the approximation $E(I_B, T_s, B) - E(I_B, T_b, B) - \bar{E} \approx (I_B - I_{co}(\lambda, T_b, B))/\alpha(I_B, \lambda, T_b, B)$ to obtain

$$PCR = \frac{1}{2}\text{erfc}\left[\frac{I_B - I_{co}(\lambda, T_b, B)}{\sqrt{2}\sigma(I_B, \lambda, T_b, B)\alpha(I_B, \lambda, T_b, B)}\right] \tag{13}$$

This is a modification of Eq.(9) for the case of a narrow wire with a detection current that does not depend on y-coordinate across the wire. If the width of the PCR curve is narrow relative to the de-pairing current, we may keep only the first term in a series expansion of $E(I_B, T_s, B) - E(I_B, T_b, B) - \bar{E}$, effectively assuming σ and α are independent of bias current. Deviations of PCR from an ideal complimentary error function thus reflect either specific features of Fano fluctuations in the current-carrying superconducting nanowire (through σ) or a strong non-linearity of the SNSPD response (through α).

The slope of the PCR curve at I_{co} is determined by the product of σ and α and can be affected by changes in photon energy, bath temperature or applied magnetic field. As seen in Eq.(11), an increase in E_λ alone, with all else being equal, would increase σ, resulting in a more gradual slope in the PCR vs. I_B curve at I_{co}. However, changing the photon energy can also change F_{eff}, ε and α.

In other superconducting sensors with no significant disorder, such as superconducting tunnel junctions and many types of microwave kinetic inductance detectors, ε is typically a constant. In these other detectors, the temperature of the hotspot does not rise close to the critical temperature T_C even for rather large photon energies of a few eV—or even a few keV, depending on device design. The transport current is small compared to the de-pairing current and the order parameter stays close to its value at zero current and temperature, $\Delta(0,0)$. Therefore, the energy required to generate a pair of quasiparticles is constant during the downconversion process: $\varepsilon = 1.75\Delta(0,0)$.

The situation in a strongly disordered, current-carrying nanowire is quite different. Before and just after photon absorption, the order parameter at a given bias current I_B and bath temperature T_B is $\Delta(I_B, T_B)$, which is smaller than $\Delta(0,0)$ (depending mostly on the

value of the bias current if bath temperature is not too close to T_C). As down-conversion progresses, the hotspot temperature T increases, reducing the order parameter—and hence the energy required to generate a quasiparticle pair. As a result, some low-energy phonons emitted shortly after photon absorption do not initially have enough energy to generate quasiparticles. If these phonons survive and remain in the superconducting film long enough, eventually $\Delta(I_B, T)$ is reduced to the point that these early-generation phonons gain pair-breaking capability. This happens if down-conversion and thermalization times are faster than the phonon escape time from the film.

As the hotspot temperature approaches the critical value T_s, the order parameter remains nonzero, and ε asymptotically approaches a much lower value $\varepsilon \to 1.75\Delta(I_B, T_s) < 1.75\Delta(I_B, T_B)$. If the cutoff current shifts to a lower value (because of increasing photon energy or bath temperature, for example), then T_s will increase and ε will decrease resulting in a steeper slope in the PCR vs. I_B curve at I_{co}.

As discussed in the previous section, in WSi nanowires, F_{eff} is dominated by J^1, which is not expected to depend strongly on E_λ or T_b. In larger-gap NbN, by contrast, σ_1 is more likely to be large enough that changes in the Fano factor F could influence F_{eff}. Unfortunately, the only available estimates for F were obtained by Monte-Carlo simulations in the absence of transport current[6,7]. As T approaches T_s, smearing of the quasiparticle density of states in a current-carrying wire becomes quite substantial. The distribution of non-equilibrium quasiparticles over the interval $\Delta \leq \epsilon \leq 3\Delta$ becomes flatter, and F (being proportional to the variance of their energy) is likely to increase its contribution to F_{eff}.

The other factor, α, depends more strongly on I_B, because it is determined by a highly non-linear function of bias current:
$$\alpha^{-1}(I_B, \lambda, T_b, B) = \frac{\partial\left(E(I_B, T_s, B) - E(I_B, T_b, B)\right)}{\partial I_B}\bigg|_{\bar{E}},$$
neglecting any potential dependence on $\bar{E}$ of I_B. It can be analyzed only numerically.

Each of these four factors (F_{eff}, ε, E_λ and α) can vary with T_b, λ and B in different ways. Studying how the slopes of $PCR(I_B)$ curves are affected by changing each of these external variables should therefore give insight into the role of each factor. Whether this slope increases, decreases or stays constant will depend on whether changes to F_{eff}, ε, E_λ or α are dominant. Such transformations have been observed in experiments, and will be discussed in Section III A.

E. The effect of Fano fluctuations on the shape of PCR curves in wide SNSPDs

In wide SNSPDs, the sensor response depends on the y-coordinate of the absorption site across the
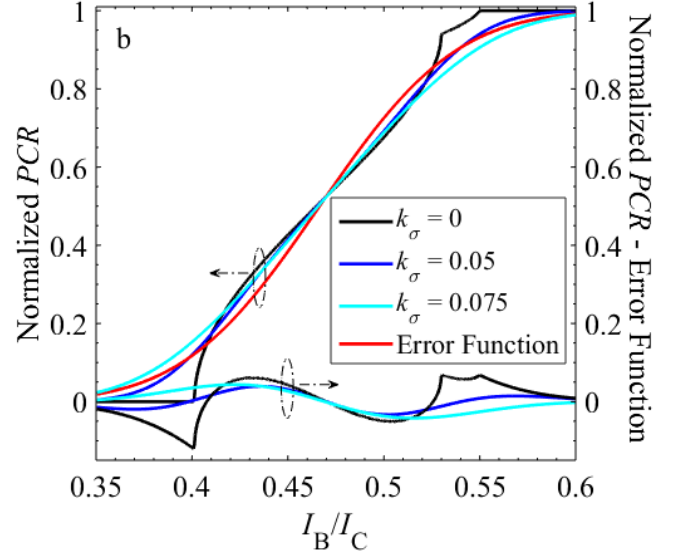

FIG. 3: (a) Schematic predictions of I_{det} vs transverse coordinate y showing bell-shaped (upper solid curve) and w-shaped (lower solid curve) profiles. The dotted curves illustrate the variations expected at each position resulting from Fano fluctuations. The two sections with width $w/2$ (or $w/2 + \delta w/2$ if fluctuations are taken into account) form the part of the nanowire of total width w (E, T_b, B) in expression (9), where vortex generation results in formation of a normal domain across the wire (b) Predicted PCR assuming a w-shaped I_{det} profile in an ideal SNSPD without Fano fluctuations (black), along with the best-fit error function shape (red), and two shapes smeared by Fano fluctuations (blue and cyan) with variances differing by a factor 1.5. Curves of the same colors at the bottom show differences between each PCR curve and the best-fit error function.

nanowire. In a spatially homogeneous nanowire, this dependence can be expressed in terms of position-dependent detection current $I_{det}(y)$. Fig.3a depicts two shapes that are discussed in the literature: bell-shaped[16] and w-shaped[19,36]. For illustration, we take the w-shaped profile depicted in Fig.3a with an average detection current of half the critical de-pairing current and a difference between maximum (I_{det}^{max}) and minimum (I_{det}^{min}) detection currents of ~0.1 of this current. The black curve in Fig.3b shows that, in the absence of fluctuations, the PCR curve has an unusual shape, with an abrupt transition (and infinite derivative with respect to current) at the onset of counts ($I_B \sim 0.4I_c$). As the bias increases above the value of I_{det} at the center of the wire ($I_B \sim 0.53I_c$), there is another sharp feature in the PCR curve as the derivative transitions from being infinite on the lower-current side to finite for higher currents. The closest fit error function (red curve) is shown on the same graph, as is the difference between the red and black curves (lower black curve).

PCR curves that more accurately reflect experimental data can be obtained by modifying the w-shaped profile model to account for Fano fluctuations. To do

this, we replace $\sigma I'_{det}(y, \chi E_\lambda, T_b, B)$ in Eq. (9) by $\left(\frac{\sigma}{E_\lambda} \frac{\partial \ln I_{det}}{\partial \ln E_\lambda} \right) I_{det}(y)$ and introduce $k_\sigma = \left(\frac{\sigma}{E_\lambda} \frac{\partial \ln I_{det}}{\partial \ln E_\lambda} \right)$. The blue and cyan curves in Fig.3b show the "smearing" effect of Fano fluctuations for $k_\sigma = 0.05$ and $k_\sigma = 0.075$ respectively, while the lower curves of the same color plot the differences between the smeared responses and the best fit error function. At $k_\sigma = 0.05$, the PCR curve is noticeably smoother than the black curve, yet its shape still significantly differs from the error function: at low bias currents it is smaller, close to saturation it is higher, and there are three inflection points in the transition region. Only with a further increase to $k_\sigma = 0.075$ does the PCR curve acquire a shape approaching an error function.

As a result, the observation of smooth error function-like sigmoidal shapes in wide-wire SNSPDs indicates a much weaker co-ordinate dependence than shown in Fig.3a. Such a weak co-ordinate dependence on its own cannot be responsible for the observable width of the transition region, and $\Delta I_B \gg I_{det}^{max} - I_{det}^{min}$. In this case the shapes of PCR curves of wide-wire SNSPDs will closely resemble the PCR curves of narrow-wire SNSPDs. Spatial inhomogeneities connected to vortex initiation will also be smoothed out by Fano fluctuations, which also determine the width of the transition region, ΔI_B. Moreover, the hot belt and hot spot models[36] will further merge with appropriate replacements $T_s \leftrightarrow T^*$, $I_{co} \leftrightarrow I_{det}$ and $\alpha(I_B, \lambda, T_b, B) \leftrightarrow I'_{det}(y, \chi E_\lambda, T_b, B)$.

III. COMPARISON WITH EXPERIMENT

A. PCR vs I_B curves

For comparison with experiment, we have chosen the PCR vs I_B curves of a WSi SNSPD measured at several excitation wavelengths and bath temperatures[30] shown in Fig.4. We use these data for several reasons. First, all experiments were performed using the same high-quality device where all count rates exhibited saturation below the switching current. Second, there are four different experiments, two that measure the single-photon detection efficiency, and two that interrogate the time-delayed two-photon response. The latter measurements probe the relaxation of a hot spot created by one photon as a function of excitation wavelength and bath temperature. Further experiments were also conducted to obtain the material parameters[30]. In our prior work, no attempt was made to use these data for simulating and interpreting the shapes of PCR in the transition region; the theoretical $PCR(I_B)$ was modeled as an ideal step function for single-photon detection or a rectangular-shaped $PCR(t_D)$ for the time-delayed two-photon experiments, where t_D is the time delay between two successive photon pulses[31].

Here, by contrast, we show that a model including Fano fluctuations gives more realistic predictions for both
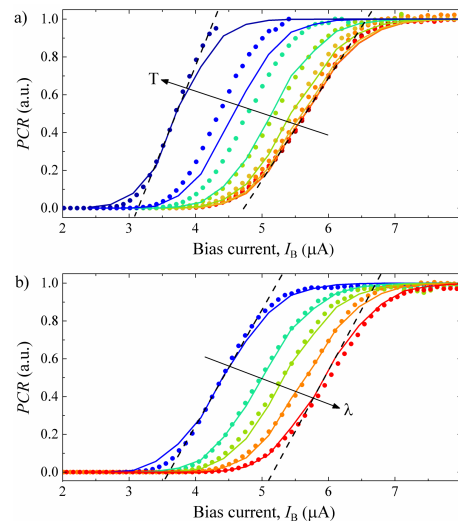

FIG. 4: Normalized photon count rate (PCR) for a WSi SNSPD operated in the single-photon detection regime for a series of (a) bath temperatures from 250 mK to 2 K with an increment 250 mK and (b) wavelengths λ=1200, 1350, 1450, 1550 and 1650 nm. Solid curves are theoretical simulations and solid circles are experimental results. Dashed lines indicate the slopes of the outer PCR curves. All theoretical curves in (a) and (b) were fit simultaneously with only 4 fit parameters: $F_{eff} = 1.3$, $\bar{\chi} = 0.32$, $\tau_0 = 5$ ns and I_{sw}/I_{dep}=0.62.

$PCR(I_B)$ and $PCR(t_D)$, and can provide new insight into the physics underlying detector operation. In this Section, we test predictions of such a model connecting dynamic Fano fluctuations with various functional forms of photon count rates observed experimentally. Simulations are based on the hotspot dynamics model developed in[31], modified to include Fano fluctuations.

Figure 4a shows the experimental and fitted PCR vs I_B curves at several temperatures. The material parameters used are those determined in our previous work:[30] WSi wire dimensions 5 nm thick and 130 nm wide, T_C=3.7 K, square resistance 476 Ω, $N(0) = 20.3 \times 10^{21}$ eV^{-1}cm^{-3}, and $D = 0.75$cm^{2}s^{-1}. To model the hot belt, we use two fitting parameters: the average energy conversion efficiency $\bar{\chi}$ and the characteristic electron-phonon relaxation time τ_0—the latter being relevant only in the time-delayed two-photon experiments. To this, we add the effective Fano factor, F_{eff}, as a third fit parameter.

Despite some degree of uncertainty in material parameters such as $N(0)$, D and τ_0, these can be measured in independent experiments and are better known than the energy conversion efficiency or the Fano factor. $\bar{\chi}$ is related to phonon escape from the film, and is determined through an integral over all electrons and phonons in the down-conversion cascade. For that reason, we do not attempt to express it in terms of conventionally used phonon escape time and use it as free fitting parameter. (Alternatively, some "average" phonon escape time as a free fitting parameter can be introduced[36].)

The last remaining parameter is the critical de-pairing current, I_{dep}. In principle, it can be measured through the dependence of kinetic inductance on bias current[34]. In our previous work on this device,[30,31] no distinction was made between the measured switching current I_{sw} (which was 9.0 μA at $T = 2$K) and the critical de-paring current I_{dep}; this likely affected our fit values of $\bar{\chi}$ and τ_0. The difference between I_{sw} and I_{dep} is significant, and here we make the revision by taking a theoretical estimate for de-paring current density[37], $I_{dep} = 1.491N(0)e[\Delta(0)]^{3/2}[D/\hbar]^{1/2}Wd$, obtaining $I_{dep} = 14.6$ μA and $I_{sw}/I_{dep} = 0.62$. For evaluation of σ_2 we used $J^1 = 1.3$. This is consistent with calculated values of J^1 for WSi on a-SiO$_2$, which range between 1 to 1.5 (for $\eta = 0.5$) taking τ_0 in the interval 5 to 10 ns. $l_{pe,D}$ varies in the limits from 2.6 nm to 5.2 nm. Note that there is no information in the literature about the strength of elastic scattering of phonons in amorphous WSi films. For comparison, in a 6.9 nm-thick amorphous SiO$_2$ film, the phonon mean free path defining heat conductivity at $T > 50$ K is comparable to the film thickness[38].

The qualitative agreement between theory and experiment in Fig.4a is good. The simulated curves for the whole range of bath temperatures from 0.25 to 2 K are close to the experimental results. The simulations also reproduce the increase in slope of the PCR curve with increasing bath temperature. This feature is clearly seen in the experimental data and is an extra consistency check of our kinetic model.

Also consistent with the experimental data is the group of simulated PCR curves for different photon wavelengths at fixed bath temperature, which have almost identical slopes. We used the same set of fitting parameters as in Fig.4a, fixing the bath temperature and allowing λ to change. Steeper slopes at smaller bias currents (higher T_s in a fixed-λ experiment) originate in the nonlinear $E(I_B, T_s, B) - E(I_B, T_b, B)$ dependence. The same nonlinearities are effective for a similar range of currents in determining the shape of $PCR(I_B)$ curves at fixed bath temperature and variable λ. However, in the second experiment, shown in Fig. 4b, the effect of the nonlinearity is nearly balanced by the square-root dependence of the variance σ on photon energy. As a result, the corresponding slopes remain almost unchanged, as expected from the model.

B. The role of static non-uniformities

As we have shown, dynamic Fano fluctuations are expected to be dominant in the absence of other fluctuations. Nonetheless, static non-uniformities of the nanowire itself may also play a role in broadening the PCR curves. Such inhomogeneities could result from geometric imperfections (non-uniform width or thickness) or from spatial variations in film structure and composition. These static non-uniformities contribute to spatial variations of critical current and critical temperature, resulting in local variations of detection threshold, E^*, and thus detection current, I_{det}.

Fortunately, the effects of spatial inhomogeneities and Fano fluctuations can be separated. To illustrate this, we will discuss a simple 1-D model, assuming that the de-pairing current exhibits long range random fluctuations along the length of the nanowire (the x-direction), with a mean value $\overline{I_{dep}}$ and variance ΔI_{dep}. We also assume that the detection current within the hot belt model remains a fixed ratio of the de-pairing current for a particular photon wavelength λ for all x, so that $I_{det}(x, \lambda) = r(\lambda)I_{dep}(x)$. (For simplicity, we assume T_b and B are fixed.) This leads to fluctuations of $I_{det}(x, \lambda)$ about a mean value $I_{co}(\lambda)$, which marks the midpoint on the PCR transition for this wavelength. The width of the transition is then $\Delta I_B(\lambda) \propto r(\lambda)\Delta I_{dep}$.

Within this model, the ratio

$$\frac{\Delta I_B(\lambda)}{I_{co}(\lambda)} = \frac{\Delta I_{dep}}{\overline{I_{dep}}} \qquad (14)$$

remains fixed for all λ. As a result, a shorter-wavelength photon ($\lambda' < \lambda$) with a smaller cutoff current will have a proportionally narrower transition width. The ratio of cutoff currents at the two wavelengths should then equal the ratio of the transition widths:

$$\frac{I_{co}(\lambda)}{I_{co}(\lambda')} = \frac{\Delta I_B(\lambda)}{\Delta I_B(\lambda')} = \frac{r(\lambda)}{r(\lambda')} > 1 \qquad (15)$$

This is quite different from our predictions based on Fano fluctuations discussed in the previous section.

Comparing experimentally measured ratios of cut-off currents and transitions widths should thus give insight into whether spatial fluctuations or Fano fluctuations dominate. Unfortunately, our data in Fig.4(b) do not span a large enough range of photon energy for a definitive test in our device. Recent measurements over a much wider range from 750 nm to 2050 nm were reported for an amorphous MoSi SNSPD[39], as shown in their Fig.2. The transition width, which they defined as $\Delta I_B = I_B^{80\%} - I_B^{20\%}$, changed from ~1.0 to ~1.7 μA when λ increased from 750 to 2050 nm. The ratio of widths is $\Delta I_B(2050\text{nm})/\Delta I_B(750\text{nm}) \approx 1.7$, while the ratio of cut-off currents is $I_{co}(2050\text{nm})/I_{co}(750\text{nm}) \approx 3.8$ as seen from Figs. 2 and 4 of Ref.[39]. These two ratios differ by more than a factor of two, indicating that Fano fluctuations dominate over spatial non-uniformities in determining the transition width. In that work, the width also showed signs of saturation at $E_\lambda \geq 1$ eV, which is in line with an increasing role of Fano fluctuations. For the highest photon energy reported in[39] (from the inset of their Fig.4), we estimate $\Delta I_B/I_{co} \sim 25\%$. This means that if the transition width were due entirely to spatial non-uniformities, then for 25% of the area $|\Delta I_{dep}|/\overline{I_{dep}} > 12.5\%$, while in 75% of the nanowire area I_{dep} varies in the range $\pm 12.5\%$ about the mean value. MoSi, like WSi, is an amorphous film; as a result,

film uniformity is typically much higher than in policrystalline materials such as NbN. Thus, it would be surprising if such a large spatial variation were present in MoSi or WSi.

C. P_{click} vs t_D curves

We have shown that Fano fluctuations play an important role in smearing the detection threshold. This conclusion holds regardless of the ultimate detection mechanism, which primarily affects the magnitude of the threshold energy E^* and correspondingly the effective T_s. Here we discuss the role of Fano fluctuations in determining the hotspot relaxation dynamics. As reported in Ref.[30], we coupled optical pulse pairs separated by a variable delay t_D to an SNSPD operating in the two-photon regime. In the two-photon detection regime, a photoresponse pulse can be efficiently triggered only if two photons generate two overlapping hotspots. As shown in Fig.5, we measured the probability of a response pulse, or click (P_{click}), as a function of t_D for several bias currents. The P_{click} vs t_D curves have Lorentzian shapes and become wider as the bias current is increased. We defined the hotspot relaxation time as the half width at half maximum of each Lorentzian curve[30].

In an ideal, fluctuation-free model where the PCR vs I_B curve is a step function, each P_{click} vs t_D curve will have a rectangular shape with a width determined by the hotspot relaxation time[31]. In this section, we show that Fano fluctuations will smooth the sides of these rectangles, transforming them to Lorentzian-shaped curves. Neglecting diffusive expansion[31], we let the first pulse at $t = 0$ deposit an energy E with probability $P(E)$, which creates a hotspot with initial temperature $T_{ex} = T(E, T_b, I_B)$. Subsequently the hotspot relaxes, and its temperature follows the functional dependence $T(E, T_b, I_B, t)$. The latter can be found as a solution of the kinetic equation[31]. At an instance of time $t = t_D$, the hotspot energy, E_{HS}, thus decreases to $E_{HS}(T(E), T_b, I_B, t_D)$. Then the normalized two-photon P_{click} becomes

$$PCR(t_D) = \int_0^\infty \mathrm{d}E P(E) \int_{E^* - E(T(E), T_b, I_B, t_D)}^\infty \mathrm{d}E' P(E') =$$
$$\frac{1}{2} \int_0^\infty \mathrm{d}E P(E) \mathrm{erfc} \left[\frac{E(I_B, T_s) - E(T(E), T_b, I_B, t_D) - \bar{E}}{\sqrt{2}\sigma} \right]$$

(12)

Fig.5b shows the simulated shapes of $P_{click}(t_D)$ for several different values of bias current using the following parameters: $F_{eff} = 1.3$, $\bar{\chi} = 0.32$, I_{sw}/I_{dep}=0.68 and $\tau_0 = 5.0$ ns.

The excellent agreement between experiment and theory displayed in Fig.5 indicates that Fano fluctuations play a dominant role in shaping the photoresponse $P_{click}(t_D)$, and provides further evidence in favor of our prior theoretical model[30,31]. In short, this model predicts
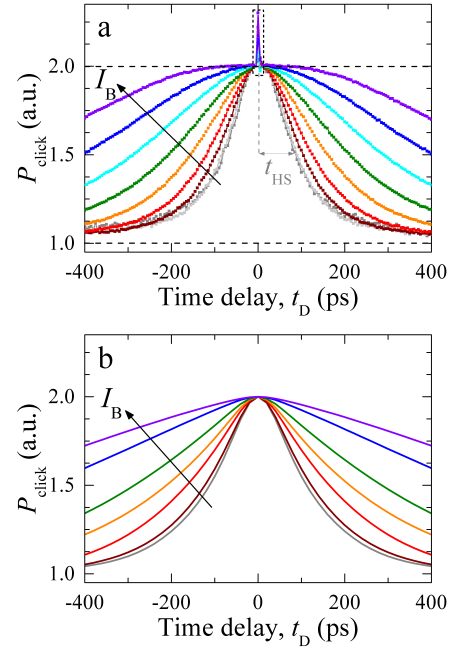

FIG. 5: Normalized click probability P_{click} as a function of time delay t_D for a series of bias currents. (a) Experimental data taken at a bath temperature of 0.25 K for photons of wavelength λ =1550 nm. (b) Simulations. The entire set of theoretical curves was generated using the same set of fit parameters as in Fig.4 except I_{sw}/I_{dep}=0.68.

that in amorphous WSi nanowires, hotspot relaxation is dominated by self-recombination. While the simulated curves in Fig.5 are well matched to the experimentally observed Lorentzians over the range of time delays shown here, their tails differ from the experimental data. The simulated tails fall between that of Lorentzian and Gaussian. It is possible that diffusion makes most of its contribution at the tails of $PCR(t_D)$, causing reduced self-recombination at the periphery of the hotspot.

Simulations were done at parameter values close to our of earlier work[30,31], but assuming a switching current 32% less than the de-paring current and correspondingly a more efficient energy deposition parameter than we had previously assumed. In general, a larger difference between the switching and de-paring currents requires larger factors $\bar{\chi}$ to match theory and experiment. Physically, this means that achieving a higher critical temperature in a wire, with bias current being a smaller fraction of the de-paring current, requires more deposited energy. Also, decreasing I_{sw}/I_{dep} and increasing $\bar{\chi}$ results in a weaker dependence of the hotspot relaxation time on bias current, as evidenced by a weaker dependence of hotspot relaxation time on I_B at lower currents. This dependence becomes weaker also for larger values of τ_0.

Allowing I_{sw}/I_{dep} to be a free fitting parameter, we may shift the simulated PCR curves along the bias current axis, achieving a better fit to the experimental data.

These simulations must be considered together with the best fits in Fig.4, which required the same set of fitting parameters as for simulations in Fig.5 except for I_{sw}/I_{dep}=0.6. Achieving a good fit with the same material parameters and fixed values for I_{sw}/I_{dep}, F_{eff} and $\bar{\chi}$ is very challenging. We could have fit each separate experiment better by allowing some flexibility of each individual parameter. The fact that we can fit all the experiments reasonably well, allowing only a 12% variation of a single fit parameter (I_{sw}/I_{dep}) with the other three fit parameters fixed, shows both the validity of the model and the accuracy of the main assumptions.

D. Discussion

Our simulations of single-photon PCR curves and two-photon pump-and-probe experiments with variable time delay were based on a narrow nanowire hot-belt model. The analogous hot-belt model was claimed to be irrelevant for both NbN and WSi SNSPDs with nanowire width exceeding 150 nm[36]. Our experiments and simulations therefore allow testing of the hot-belt model predictions for a wide range of experiments and comparison to predictions of the hotspot model where we can identify expected differences. The hot-belt model is the only tested model that allows interpretation of the two-photon detection experiment. For all other experiments, it was shown that the hot belt and hotspot models predict qualitatively similar, but quantitatively different results (except for SNSPDs in external magnetic fields in a certain range of bias currents). In contrast, the agreement with experiment we show here is much closer than what could have been inferred on the assumption that the hot-belt and hotspot models work for two-photon and one-photon experiments, respectively.

The narrow-wire model should be valid provided $\tau_{th} \geq \tau_D$, where τ_{th} is the characteristic thermalisation time, controlling suppression of the gap within the initial volume, and τ_D is characteristic diffusion time across the nanowire[36]. We do not use the coherence length as the radius R_0 of the phonon bubble. This scale is not relevant for the initial state, because the radius of the phonon bubble must be exactly the same for a normal metal. We chose $R_0 = \sqrt{4Dt_d + l_{pe,D}^2}$ as the more appropriate spatial scale. Here t_d stands for the descent time for a photoelectron(hole) from the level E_1^* to the Fermi energy. R_0 thus represents the net length of the random walk that the primary photoelectron and hole perform while disposing their excess energy to phonons, creating a phonon bubble. The second term under the square root accounts for extra volume expansion due to phonons in the bubble moving on average a distance of their mean free path prior to being re-absorbed by electrons.

For WSi using $d = 5$ nm, $D = 0.75 \text{cm}^2/s$[30], $\tau_0 = 10$ ns, $\Omega_D = 34$ meV[41], $c = 3.2 \cdot 10^5$ cm/s,

$t_d = \tau_0 \frac{3E_1^*}{\Omega_D}\left(\frac{T_C}{\Omega_D}\right)^3$, $\tau_{pe,D} = \frac{\tau_0}{\gamma}\frac{T_C}{\Omega_D}$ and γ=57.6 corresponding to $T_C = 3.7$ K and $N(0) = 20.3 \cdot 10^{21} 1/\text{cm}^3\text{eV}$, we obtain for the volume of the phonon bubble $V_0 = \pi R_0^2 d$=2130 nm^3. This exceeds the initial volume used for the estimate of τ_{th} in Ref.[36]. For $\tau_0 = 5$ ns this volume becomes 958 nm^3. The energy density is therefore smaller, resulting in a lower temperature of electrons and phonons in the hotspot: $T_e = T_{ph} = 4.1T_C$ and τ_{th}=8.6 ps ($T_e = T_{ph} = 5.15T_C$ and τ_{th}=2.2 ps for $\tau_0 = 5$ ns) for absorption of a 1550 nm photon, as estimated from energy conservation.

There is currently no consensus in the literature regarding the magnitude of τ_0, with recent measurements of magnetoresistance[40] yielding τ_0=1.9 ns. We have chosen τ_0 to be in the range of 5-10 ns for two reasons. This value fits the measurements of electron-phonon relaxation time[41] over the low temperature range. It also better fits the expected magnitude of τ_0 inferred from scaling according to the Ω_D^2/T_C^3 law, which must work during the formation of the phonon bubble, when effects of disorder on electron-phonon interactions are not important. Phonon escape from the SNSPD film and diffusive expansion during thermalisation both reduce the energy density within the volume filled with non-equilibrium excitations, resulting in a further slowdown of thermalization.

A more important process is likely to be diffusive expansion, which may result in a substantial increase of τ_{th}. Indeed, during the first picosecond the evolving hotspot expands to fill a volume of 4710 nm^3. Reducing energy density within the evolving hotspot results in the temperature of thermalised quasiparticles and phonons of $3.2T_C$ and $\tau_{th} > 18.1$ ps (>9.1 ps for τ_0=5 ns). The representative value for expansion time of the hotspot across the width of the wire is the diffusion time from the center of the strip, $\tau_D \sim W^2/16D \simeq 14.1$ ps. Accounting for both phonon loss and diffusion during thermalization must be done within a refined model. In the absence of such a model and in view of significant uncertainty of material parameters, the question of validity of one or the other model remains open.

The experimental data in Figs.4a and b have smooth sigmoidal shapes close to predicted error functions. Indeed, there is no evidence of coordinate-dependent response in the transition region. With any of the bell- or w-shaped coordinate-dependent responses, one expects a change in curvature at the inflection point from concave below the cutoff current ($I_B < I_{co}$) to convex above the cutoff current($I_B > I_{co}$) as shown in Fig.3. In contrast, for a narrow wire, the predicted error function shape is convex on the left and concave on the right of the inflection point.

To check whether the experimental data in Fig.4 can be approximated by error functions, in Fig.6 we show the results of fitting each curve to a simple error function, $PCR = \frac{A}{2}\text{erfc}\left(\frac{I_{co} - I_B}{\Delta I_B}\right)$, where A and ΔI_B are fitting
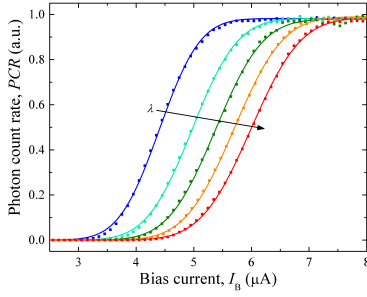
FIG. 6: Fitting PCR vs I_B for $\lambda = 1200, 1350, 1450, 1550$ and 1650 nm by error functions.

parameters that we optimize separately for each wavelength. No signs of coordinate-dependent response are seen in Fig.6. It is difficult to estimate the k_σ for the position-dependent wide-wire model, because the logarithmic derivative $\partial \ln I_{det}/\partial \ln E_\lambda$ is unknown. If we assume that this derivative is close to that for the maximum detection current, then it can be roughly estimated using the results in Fig.14 of reference[36] for photon energies corresponding to our range of wavelengths. Such an estimate yields $k_\sigma \leq 0.03$; according to our simulations in Fig3b, the specific features associated with a w-shaped profile of detection current should have been seen.

In a recent paper on MoSi SNSPDs, the PCR curves were measured and fitted with error functions for a wavelength range of 750 to 2050 nm. It was found that at low photon energies the fit agrees very well with the data. However, at high energies, the shapes of the curves starts to deviate from simple error functions[39]. The authors hypothesize that these deviations might indicate a coordinate-dependent response of the SNSPD. The observed deviations, however, are not what can be expected from a coordinate-dependent response, as shown in Fig.3b. First, the curvatures of PCR shapes on both sides of the inflection points remain consistent with a Fano fluctuation-induced homogeneous sensor response. Second, the experimental curves show smaller counts both in the lower-bias tail and on approach to the saturation level. This is not indicative of an inhomogenious response, for which on approach to I_{det}^{max} the photon counting rate should exhibit a cusp and stay above the error-function as seen in Fig.3 for $k_\sigma = 0$.

Strong Fano-fluctuations with $k_\sigma = 0.05$ and $k_\sigma = 0.075$ smear specific cusps on the curve $k_\sigma = 0$, when no fluctuations are present. However, incorporation of Fano-fluctuations fails to simulate the smaller counts both in the lower bias tail and on approach to saturation level. It is possible that the observed deviations are connected with the non-linearity of the SNSPD response given by the function α in expression (13). This non-linearity is of the same origin as the observed substantial non-linearity of the current-energy relation in MoSi[39]. The results[39] may be explained within the hotspot model provided that the detection current is only weakly dependent on the coordinates of the absorption site. The predicted width of

the transition range of PCR, $I_{det}^{max} - I_{det}^{min}$, must be much smaller than the variances describing Fano and static fluctuations. In this limit the predictions of the hotspot model for the shape of PCR vs I_B will be no different from the hot belt and both models further merge as explained in Section II.

The effects of an external magnetic field on PCR vs bias current[18,23,42,43] deserve special attention, since they can give insight into the detection mechanisms in SNSPDs[23,42]. Features due to Fano fluctuations were not accounted for in any of the previous work. There are several ways that external magnetic fields can combine with Fano fluctuations and thus cause the PCR curves to change shape. In an external perpendicular magnetic field, the threshold E^* depends on the field magnitude, as seen in (5) and (8). Both the critical current and the de-pairing energy depend on magnetic field, with the former being dominant for weak magnetic fields. With $I_c(B)$ decreasing as B increases, the obvious effect in weak fields is the shift of PCR curves towards lower currents, as observed in[23,42,43]. The magnitude of the shift depends on the exact functional dependence of $I_c(B)$.

Vodolazov $et\ al.$[23,42] observed shape transformations of the PCR curves with varying magnetic field and photon wavelength above the crossover current. Their results were interpreted on the basis of a model assuming vortex trapping by compact hotspots having a radius depending on the photon wavelength. The SNSPD response in a weak magnetic field was suggested as the definitive experiment for identification of the detection mechanism[36]. Within our model with uniform current density, there is no such a crossover. Nonetheless, the shifts may assume a more complicated pattern due to the interplay between the critical current, the de-pairing energy, and the complicated nonlinear $E(I_B, T_s, B) - E(I_B, T_b, B)$ dependence. At shorter photon wavelengths, the PCR curves shift towards lower bias, where the contribution of the magnetic field term to the de-pairing energy increases relative to the supercurrent term. A significant non-linearity of the energy-current relation was recently reported over the spectral interval 750-2050 nm[39]. A full understanding of the detection mechanisms in SNSPDs will require a more detailed study of PCR shapes through the transition range at the low current tail, near inflection points, and close to saturation, together with a thorough study of magnetic field-dependence.

Finally, Fano fluctuations are a universal factor setting the theoretical limit for the timing jitter of an SNSPD, independent of detection mechanism. There has been spectacular progress recently in improving timing jitter of NbN SNSPDs to a record level of 5 ps[44]. The FWHM is given by $\sigma_j = 2\sqrt{2 \ln 2}\sqrt{\sigma_{el}^2 + \sigma_{g\parallel}^2 + \sigma_{g\perp}^2 + \sigma_{j,N-u}^2 + \sigma_{j,Fano}^2}$, where σ_{el}, $\sigma_{g\parallel}$, $\sigma_{g\perp}$, $\sigma_{j,N-u}^2$ and $\sigma_{j,Fano}^2$ are respective variances describing electronic noise, geometric noise originating from uncertainty of absorption site position along the wire length (x-axis), geometric noise originat-

ing from uncertainty of absorption site position along the perpendicular direction (y-axis) including coordinate-dependent dynamics of normal domain initiation and growth and the effect of spatial non-uniformities and Fano-fluctuations. The first three factors can be calibrated, resulting in an estimate of the remaining contributions in the range of a few ps. The next factor is fully deterministic, depending on the transverse coordinate of the absorption site, detection model and dynamics of initiation and growth of the resistive state. One attempt was recently made on modelling $\sigma_{g\perp}$ depending on vortex dynamics[45] based on model[36] evaluating this contribution at ~ 1 ps at $\sim 0.6 I_{dep}$ rapidly decreasing to 0.1 ps on approach to I_{dep}. An SNSPD optimised for best timing jitter will operate close to saturation of the PCR curve as a function of bias current and $I_B > I_{det}^{max}$. In these conditions, the role of probabilistic factors, dynamic Fano-fluctuations and spatial non-uniformity, will be the remaining challenges to take care of in order to advance into sub-picosecond timing jitter performance. From this prospective, metallic glasses like WSi and MoSi look preferable, being more uniform with smaller $\sigma_{j,N-u}^2$, while Fano-variances $\sigma_{j,Fano}^2$ in policrystalline films like NbN, NbTiN and amorphous WSi, MoSi are likely to be comparable. The latter is plausible because of the dominant role of phonon-electron interaction determining athermal phonon mean free paths relative to grain boundary phonon scattering in policrystalline films or resonant scattering by two-level systems and local harmonic oscillators in amorphous films.

IV. CONCLUSIONS

In summary, we have shown how Fano fluctuations play a fundamental role in superconducting nanowire single-photon detectors. They are an essential factor in determining the exact shape of both single-photon photoresponse and time-delayed, two-photon photoresponse. The special features of $PCR(I_B)$ curves, such as slope transformation, positions of inflection points versus wavelength, bath temperature and magnetic field reveal a wealth of sensor physics and will do a significant service for unambiguous determination of the detection mechanisms.

V. ACKNOWLEDGEMENTS

[1] R. T. Williams, J. Q. Grim, Qi Li, K. B. Ucer, G. A. Bizarri and A. Burger, Scintillation Detectors of Radiation: Excitations at High Densities and Strong Gradients in "Excitonic and Photonic Processes in Materials" ed. Jai Singh and Richard T. Williams, Springer Series in Materials Science 203 (2015)

[2] K. J. Tielrooij, J. C. W. Song, S. A. Jensen, A. Centeno, A. Pesquera, A. Zurutuza Elorza, M. Bonn, L. S. Levitov and F. H. L. Koppens, Photoexcitation cascade and multiple hot-carrier generation in graphene, Nature Physics **9**, 248252 (2013)

[3] Justin C. W. Song, Leonid S. Levitov, Energy Flows in Graphene: Hot Carrier Dynamics and Cooling, J. Phys.: Condens. Matter **27**, 164201 (2015)

[4] J. Janesick, T. Elliott, R. Bredthauer, C. Chandler, B. Burke, "Fano fluctuations-Limited CCDs", Proc. SPIE, **0982**, 70 (1988).

[5] G.F. Knoll, Radiation Detection and Measurement, fourth ed., Wiley and Sons, 2010.

[6] M.Kurakado, Possibility of high resolution detectors using superconducting tunnel junctions, Nucl. Instr. Meth. **196**, 275(1982)

[7] N.Rando, A.Peacock, A. van Dordrecht *et al*, The properties of niobium superconducting tunneling junctions as X-ray detectors, Nucl. Instr. Meth A **313**, 173 (1992).

[8] A.Peacock, P. Verhoeve, N.Rando, A. Van Dordrecht, B. G. Taylor, C. Erd, M. A. C. Perryman, R. Venn, J. Howlett, D. J. Goldie, J. Lumley, M. Wallis, Single optical photon detection with a superconducting tunnel junction, Nature, 381, 135 (1996)

[9] B. Cabrera, R. M. Clarke, P. Colling, A. J. Miller, S. Nam, and R. W. Romani, Detection of single infrared, optical, and ultraviolet photons using superconducting transition edge sensors Appl. Phys. Lett. 73, 735 (1998).

[10] D.D.E. Martin, P. Verhoeve, A. Peacock, A.G. Kozorezov, J.K. Wigmore, H. Rogalla, R. Venn, Resolution limitation due to phonon losses in superconducting tunnel junctions, Appl.Phys. Lett. **88**, 123510 (2006).

[11] 38. Kozorezov, A. G. Wigmore, J. K. Martin, D. Verhoeve, P.; Peacock, A., Resolution limitation in superconducting transition edge photon detectors due to downconversion phonon noise, Applied Physics Letters, **89**, 223510 (2006).

[12] A.G. Kozorezov, C.J.Lambert, S.R. Bandler, M.A. Balvin, S.E. Busch, P.N. Nagler, J-P. Porst, S.J. Smith, T.R. Stevenson, J.E. Sadleir, Athermal energy loss from x-rays deposited in thin superconducting films on solid substrates, Phys. Rev. B **87**, 104504 (2013).

[13] A.E. Lita, A.J. Miller, S. Nam, Energy Collection Efficiency of Tungsten Transition-Edge Sensors in the Near-Infrared, J Low Temp Phys, 151, 125 (2008).

[14] A. D. Semenov, et al., "Quantum detection by current carrying superconducting film" Physica C 351, 349 (2001).

[15] A. Semenov, et al., "Spectral cut-off in the efficiency of the resistive state formation caused by absorption of a single-photon in current-carrying superconducting nano-strips" Eur. Phys. J. B 47, 495 (2005).

[16] A.Engel,J.Lonsky,X.Zhang, Detection Mechanism in SNSPD: Numerical Results of a Conceptually Simple, Yet Powerful Detection Model, IEEE Ttans. Appl, Superconductivity, 25, 2200407 (2015)

[17] L. N. Bulaevskii, M. J. Graf, C. D. Batista, and V. G. Kogan,Vortex-induced dissipation in narrow current-biased thin-film superconducting strips, Phys. Rev. B 83, 144526 (2011).

[18] L. N. Bulaevskii, M. J. Graf, and V. G. Kogan, Vortex-assisted photon counts and their magnetic field dependence in single-photon superconducting detectors, Phys. Rev. B 85, 014505 (2012).

[19] D.Yu. Vodolazov, Current dependence of the red boundary of superconducting single-photon detectors in the modified hot-spot model, Phys. Rev. B 90, 054515 (2014)

[20] A. N. Zotova and D. Yu. Vodolazov, Intrinsic detection efficiency of superconducting nanowire single photon detector in the modified hot spot model, Supercond. Sci. Technol. 27 125001 (2014)

[21] J. J. Renema, R. Gaudio, Q. Wang, Z. Zhou, A. Gaggero, F. Mattioli, R. Leoni, D. Sahin, M. J. A. de Dood, A. Fiore, and M. P. van Exter, Experimental Test of Theories of the Detection Mechanism in a Nanowire Superconducting Single Photon Detector, PRL, 112, 117604 (2014)

[22] A.Engel, J.J.Renema, K.Ilin, A. Semenov, Detection mechanism of superconducting nanowire single-photon detectors, Supercond. Sci. Technol. 28, 114003 (2015).

[23] D. Yu.Vodolazov, Yu. P.Korneeva, A. V.Semenov, A. A.Korneev, G. N.Goltsman, Vortex-assisted mechanism of photon counting in a superconducting nanowire single-photon detector revealed by external magnetic field, Physical Review B92, 104503(2015)

[24] A.G. Kozorezov, A.F. Volkov, J.K. Wigmore, A. Peacock, A. Poelaert, R. den Hartog, Quasiparticle-phonon downconversion in nonequilibrium superconductors, Phys. Rev. B61, 11807 (2000).

[25] B.L.Altshuler and A.G.Aronov in "Electron-electron Interactions in Disordered systems", ed. by A.L.Efros and M.Pollak, Elsevier Science Publishers B.V., 1985

[26] J-J Chang in "Nonequilibrium Superconductivity" ed. by D.N.Langenberg and A.I.Larkin, Elsevier Acince Publishers B.V. 1986

[27] A.Schmid, Electron-phonon interaction in an impure metal, Z. Phys. 259, 421 (1973)

[28] M. Yu. Reizer and A. V. Sergeev, The effect of the electron-phonon interaction of the conductivity of impure metals , Sov. Phys. JETP 65, 1291 (1987)

[29] S.B. Kaplan et al, Quasiparticle and phonon lifetimes in superconductors, Phys.Rev. B 14, 4854 (1976)

[30] F. Marsili, M. J. Stevens, A. Kozorezov, V. B. Verma, Colin Lambert, J. A. Stern, R. D. Horansky, S. Dyer, S. Duff, D. P. Pappas, A. E. Lita, M. D. Shaw, R. P. Mirin, and S. W. Nam, Hotspot relaxation dynamics in a current-carrying superconductor, Phys. Rev. B 93, 094518 (2016)

[31] A.G.Kozorezov, C. Lambert, F. Marsili, M. J. Stevens, V. B. Verma, Colin Lambert, J. A. Stern, R. Horansky, S. Dyer, M. D. Shaw, R. P. Mirin, and S. W. Nam, Quasiparticle recombination in hotspots in superconducting current-carrying nanowires, Physical Review B92, 064504 (2015)

[32] A. Anthore, H. Pothier, and D. Esteve, Density of States in a Superconductor Carrying a Supercurrent, PRL 90, 127001 (2003)

[33] J.Romijn,T. M. Klapwijk, M.J.Renne, J.E.Mooij, Critical pair-breaking current in superconducting aluminum strips far below T_C, Phys. Rev. 26, 3638 (1982)

[34] J.R.Clem, V.G.Kogan, Kinetic impedance and depairing in thin and narrow superconducting films, Phys.Rev.B 86, 174521 (2012)

[35] A.G. Kozorezov, J.K.Wigmore, D. Martin, P. Verhoeve, A. Peacock, Electron energy down-conversion in thin superconducting films, Phys. Rev.B 75, 094513 (2007).

[36] D.Yu. Vodolazov, Single-Photon Detection by a Dirty Current-Carrying Superconducting Strip Based on the Kinetic-Equation Approach, Phys. Rev. Applied 7, 034014 (2017)

[37] M.Yu.Kupriyanov and V.F.Lukichev, Sov.J.Low Temp.Phys, 6, 210 (1980)

[38] E. T. Swartz, R. O. Pohl, Thermal boundary resistance, Reviews of Modern Physics, 61, 605 (1989)

[39] Misael Caloz, Boris Korzh, Nuala Timoney, Markus Weiss, Stefano Gariglio, Richard J. Warburton, Christian Schonenberger, Jelmer Renema, Hugo Zbinden, and Felix Bussi'eres, Optically probing the detection mechanism in a molybdenum silicide superconducting nanowire single-photon detector, Appl. Phys. Lett. 110, 083106 (2017)

[40] X.Zhang,A.Engel,Q.Wang,A.Schilling,A.Semenov,M.Sidorova,H.-W.Hbers,I.Charaev,K.Il'in, and M.SIegel, Characteristics of superconducting tungsten silicide W_xS_{-1-x} for single photon detection, Phys.Rev.B 94, 174509 (2016)

[41] M.Sidorova, A.Semenov, A.Korneev, G.Chulkova, Yu.Korneeva, M.Mikhailov, A.Devizenko, A.Kozorezov, G.Goltsman, Electron-phonon relaxation time in ultrathin tungsten silicon film, arXiv:1607.07321

[42] A. A. Korneev, Y. P. Korneeva, M. Y. Mikhailov, Y. P. Pershin, A. V. Semenov, D. Y. Vodolazov, A. V. Divochiy, Y. B. Vakhtomin, K. V. Smirnov, A. G. Sivakov, A. Y. Devizenko, and G. N. Goltsman, Characterization of MoSi Superconducting Single-Photon Detectors in the Magnetic Field, IEEE Transactions on Applied Superconductivity, 25, 6975120 (2015).

[43] J. J. Renema, R. J. Rengelink, I. Komen, Q. Wang, R. Gaudio, K. P. M. opt Hoog, Z. Zhou, D. Sahin, A. Fiore, P. Kes, J. Aarts, M. P. van Exter, M. J. A. de Dood, and E. F. C. Driessen, The effect of magnetic field on the intrinsic detection efficiency of superconducting single-photon detectors, Appl. Phys. Lett. 106, 092602 (2015).

[44] B. Korzh et al. private communication, manuscript in preparation.

[45] Hao Wu, Chao Gu, Yuhao Cheng and Xiaolong Hu, Vortex-crossing-induced Timing Jitter of Superconducting nanowire single photon detectors, CLEO2017 (2017)